Numerical evidence for a novel non-axisymmetric bubble shape regime in square channel Taylor flow

Martin Wörner

Karlsruhe Institute of Technology (KIT), Institute of Nuclear and Energy Technologies,
P.O. Box 3640, 76021 Karlsruhe, Germany
martin.woerner@kit.edu

Keywords: Square channel, Taylor flow, transition to annular flow, numerical simulation

Abstract

In this paper we present numerical investigations of co-current downward Taylor flow in a square vertical mini-channel by a volume-of-fluid method. The focus is on the shape of the front and rear meniscus at different values of the capillary number, which is here in the range $0.04 \le Ca \le 0.66$. At low values of Ca the bubble tip and rear adopt a hemispherical shape. With increase of Ca the curvature of the front meniscus increases while that of the rear meniscus decreases. This behavior is qualitatively similar to that in circular capillaries. For the highest value of Ca we find a novel regime in a square channel, where the bubble tip and body are axisymmetric, whereas the rear meniscus is not axisymmetric but shows symmetry with respect to the mid-planes and diagonals of the channel. We show that this break of symmetry is related to the pressure distribution in the liquid phase, which is non-uniform in cross-sections close to the bubble rear with the highest values occurring in the channels corners. Results for the evolution of the bubble shape during the transition from Taylor flow to annular flow are also presented.

Introduction

Taylor flow is a special kind of slug flow in small channels, where the liquid slugs which separate the elongated bullet-shaped bubbles (Taylor bubbles) are free from gas entrainment. Taylor flow occurs in micro-fluidic devices for applications in life sciences, material synthesis and chemical process engineering (Günther & Jensen, 2006; Kreutzer et al., 2005). The hydrodynamics of Taylor flow is mainly governed by two non-dimensional groups, the capillary number $Ca \equiv \mu_L U_B / \sigma$ and the Reynolds number $Re \equiv \rho_L D_h U_B / \mu_L$. Here, U_B is the magnitude of the bubble velocity, μ_L and ρ_L are the liquid viscosity and density, respectively, σ is the coefficient of surface tension and D_h is the channel hydraulic diameter.

In vertical round channels, the bubble shape is always axisymmetric, whereas for co-current upward flow in square vertical channels the bubble shape is axisymmetric for $Ca > 0.04$ and non-axisymmetric for $Ca < 0.04$ (Thulasidas et al., 1995). Recently, we used an in-house computer code based on the volume-of-fluid method and performed a computational study of the co-current downward Taylor flow of nitrogen bubbles in a viscous liquid (squalane) in a square mini-channel for capillary numbers in the range $0.04 \le Ca \le 0.66$ (Keskin et al., 2010). We compared the computed steady bubble shape with experimental flow visualizations obtained by a high speed CCD camera and found good agreement. The experimental and numerical results show both an increase/decrease of the curvature at the front/rear meniscus as the capillary number increases.

In the present study we investigate the shape of the front and rear meniscus for co-current downward Taylor flow in a square channel for varying values of the capillary number in more detail. At the highest value of Ca, we find a novel steady bubble shape regime, where the bubble tip and body are axisymmetric while the rear of the bubble is not. In an axial cross-section close to the rear meniscus, the bubble shape adopts a square with rounded corners. To the best of our knowledge, this regime has not been found in experiments or numerical simulations so far. Here, we show that this break of symmetry from an axisymmetric state to one with mid-plane and diagonal symmetry is related to the pressure distribution in the liquid film surrounding the bubble and has its origin in a substantial cross-sectional variation of the pressure in the film and corner region of the square channel. Finally, we investigate in this paper the transient evolution of the bubble shape that occurs in a square mini-channel when there is a transition from Taylor flow to annular flow.

Computational set-up

In this section we give a short description of the numerical method and the computational set-up. The time-dependent three-dimensional computations are performed with an in-house computer code, called TURBIT-VOF. This code solves the Navier-Stokes equation with surface tension term in non-dimensional single field formulation for two incompressible Newtonian fluids with constant viscosity and coefficient of surface tension on a regular staggered Cartesian grid by a finite volume method. All spatial derivatives are approximated by central differences. Time integration is performed by an explicit third order Runge-Kutta method. A divergence free velocity field at the end of each time step is enforced by a projection method, in which the resulting Poisson equation is solved by a conjugate gradient technique. The dynamic evolution of the interface is computed by an un-split volume-of-fluid method with piecewise planar interface reconstruction. For further details about the governing equations and the numerical method we refer to Sabisch et al. (2001) and Öztaskin et al. (2009).

For the computational set-up, we follow the procedure of our previous papers and consider one unit cell, which consists of one gas bubble and one liquid slug. We use in axial (vertical) direction periodic boundary conditions to mimic the influence of the trailing and leading bubble in Taylor flow. No-slip boundary conditions are applied at the four lateral walls of the square channel. In accordance with the experiments, the inner dimensions of the square channel are 1 mm × 1 mm. The axial length of the unit cell L_{uc} is either 4 mm or 6 mm. In the former case the uniform grid consists of 80 × 320 × 80 cubic mesh cells, while in the latter case the number of grid cells is 80 × 480 × 80. So in total up to about $3 \cdot 10^6$ mesh cells are used and typically a few 10,000 up to 100,000 time steps are computed.

In accordance to the experimental results reported in Bauer (2007) and Keskin et al. (2010) we use as continuous liquid phase squalane ($C_{30}H_{62}$) while the disperse gas phase is nitrogen. These experiments were performed at a pressure of 20 bar. The corresponding fluid properties of nitrogen used in the simulations are ρ_G = 23.6 kg/m^3 and μ_G=0.01804 mPa·s. Since the physical properties of squalane at a pressure of 20 bar are not available to our knowledge, we use the known (constant) properties at standard conditions which are ρ_L = 802 kg/m^3, μ_L=0.029 Pa·s, and σ = 0.0286 N/m. Thus, the viscosity of squalane is about 30 times higher than that of water.

The initial phase distribution of the simulations was defined by placing an elongated axisymmetric bubble of given volume on the channel axis. By this procedure the gas hold-up ε is fixed. The initial velocity field for both phases was given by fluids at rest, or, to save CPU time, by a constant axial velocity, or by a parabolic axial velocity profile within the channel cross-section (which was axially uniform). Starting from these initial conditions, the flow is driven by a prescribed constant source term in the axial momentum equation which corresponds to the axial pressure drop along the unit cell. In the course of the simulation, the evolution from the initial velocity field and prescribed bubble shape toward a fully developed Taylor flow is computed. The latter is assured by recording the mean axial gas and liquid velocities in the computational domain and continuing the simulation till both velocities approach constant terminal values. This final steady bubble shape corresponds to a certain (constant) bubble velocity and capillary number *Ca*. The Reynolds number *Re* is related to the capillary number by $Re = La \cdot Ca$, where $La \equiv \sigma \rho_L D_h / \mu_L^2$ is the Laplace number, which is constant here (La = 27.27). Furthermore, the Weber number is given by $We = Ca \cdot Re = \rho_L D_h U_B^2 / \sigma$.

Results and Discussion

Bubble shape in numerical simulations

In Figure 1 we show the steady bubble shape at different values of *Ca* as computed by Keskin et al. (2010). The displayed bubble shape does not correspond to a certain iso-surface of the liquid volume fraction but is obtained as follows. For each mesh cell that contains both phases the center of area of the plane which represents the interface in this mesh cell is computed. The centers of area of such planes in neighboring mesh cells that contain an interface are then connected to form triangles or quadrangles so that a closed surface is obtained.

From Figure 1 we observe that with increase of the capillary number the front of the bubble becomes more pointed while the bubble rear becomes more flat (see also Keskin et al., 2010). This result is in agreement with the numerical study of Taha & Cui (2006) who found that in a square channel a single Taylor bubble acquires spherical ends at low values of *Ca*, while the back of the bubbles changes from convex to concave at high *Ca*. This behavior is similar to circular channels (Martinez & Udell, 1989; Giavedoni, & Saita, 1999).

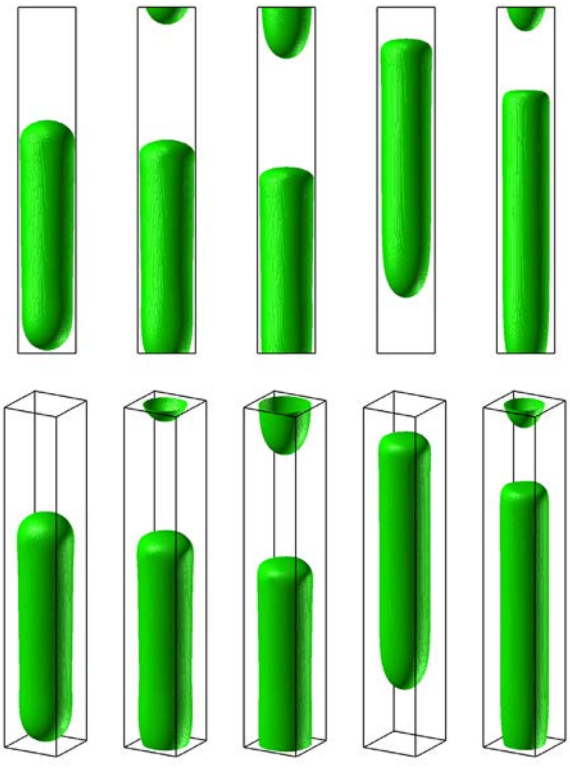

Figure 1: Side view (top) and perspective view (bottom) of computed steady bubble shape for L_{uc} = 6 mm and ε = 0.4 for five different values of the capillary number. From left to right the values of (*Ca; Re)* are (0.045; 1.22), (0.117; 3.19), (0.17; 4.64), (0.25; 6.81), (0.491; 13.4). (For further details about the simulations see Keskin et al., 2010). The solid lines indicate the size of the computational domain.

Taylor (1961) showed for a circular pipe that at small values of the capillary number the streamlines in the liquid slug show a recirculation pattern in a frame of reference moving with the bubble, while at large *Ca* so-called bypass flow occurs. Thulasidas et al. (1997) found experimentally that for co-current upward flow in a square channel this transition to bypass flow occurs for $Ca \approx 0.47$. The highest capillary number in the simulations of Keskin et al. (2010) is obtained for case 4_20_B (in this case denomination the first and second numbers indicate the axial length and the gas-holdup while the letter refers to different values of the pressure drop). For this case it is $L_{uc} = 4$ mm, $\varepsilon = 0.2$, $Ca = 0.655$ and $Re = 17.86$. It is interesting to note that thought this value is higher than 0.47, there is now bypass flow because it is $\psi \equiv U_B / J_{tot} = 1.96 < 2.096$ (see discussion in the next subsection). This suggests that the transition from recirculation flow to complete bypass flow occurs in downward flow at higher values of *Ca* than in upward flow. This conjecture is supported by Fig. 5 in Kececi et al. (2009), where ψ is displayed as function of *Ca* and numerical results for upward and downward flow are compared. This figure shows that for a given value of *Ca*, ψ is higher for upward flow than for downward flow.

In Figure 2 we show the bubble shape for case 4_20_B. This figure shows that the rear of the bubble is flat. At the axial position of the bubble, where the liquid film is thinnest and the bubble diameter is largest, the bubble shape is axisymmetric. At the rear of the bubble, however, this symmetry is lost. Figure 2 b) shows that the red line which denotes the position of the interface in a cross-section close to the bubble rear is not a circle but adopts the shape of a square with rounded corners. Thus, at the rear of the bubble the interface is not axisymmetric. Instead, there is symmetry with respect to the two mid-planes and diagonals of the square channel. To the authors knowledge this behavior has not been observed so far neither in experiments nor in numerical simulations. While the measurements of the three-dimensional shape of the rear meniscus of a moving Taylor bubble is a difficult subject by itself, it is further complicated by the fact that the axial extension of the non-axisymmetric shape reported here is only about 50 µm.

Theoretical analysis of local interface curvature

In this subsection we investigate the reasons for the shape of the rear meniscus as displayed in Figure 2 b). To this end we consider the dynamic boundary condition at the interface, i.e. the local force balance between pressure, viscous stresses and surface tension. Here, we are only interested in the projection of this dynamic boundary condition in direction of the unit vector $\mathbf{n}_i$, which is normal to the interface and points into the continuous liquid phase. Then it is

$$p_{L,i} - p_{G,i} + \tau^{\perp}_{L,i} - \tau^{\perp}_{G,i} = \sigma\kappa \tag{1}$$

with κ being twice the mean local interface curvature

$$\kappa = 2H = 1/R_{min} + 1/R_{max} \tag{2}$$

Thus, by virtue of Eq. (1) at any point on the bubble surface, the local curvature of the interface, κ, is related to the pressure p and normal viscous stress $\tau^{\perp}$ on both sides of the interface. For a Newtonian fluid, the normal viscous stress at the liquid and gas side of the interface is given by

$$\tau^{\perp}_{L,i} = \mu_L \left(\nabla\mathbf{v}_L + (\nabla\mathbf{v}_L)^T \right) : \mathbf{n}_i\mathbf{n}_i \tag{3}$$

$$\tau^{\perp}_{G,i} = \mu_G \left(\nabla\mathbf{v}_G + (\nabla\mathbf{v}_G)^T \right) : \mathbf{n}_i\mathbf{n}_i \tag{4}$$

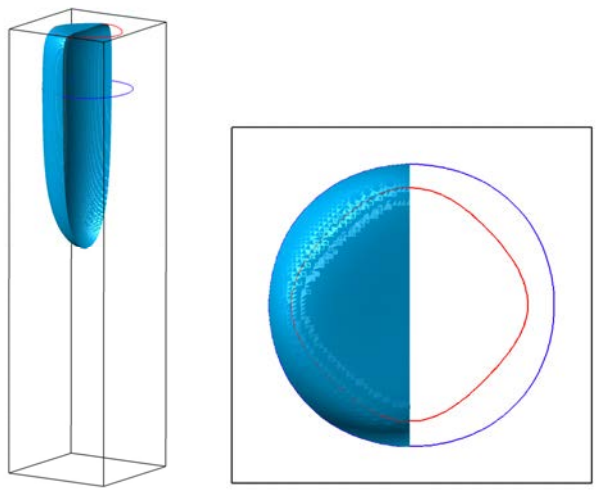

Figure 2: Bubble shape for case 4_20_B in a) perspective view and b) view from behind (only one half of the bubble is shown). The two lines indicate the bubble shape in an axial cross-section in the middle of the bubble (blue line) and very close to the bubble rear (red line).

An evaluation of the local pressure field shows that the pressure in the bubble is constant (see also Figure 3). Therefore, we assume $p_{G,i} = p_B = \text{const}$. In the present simulations, the ratio between the gas and liquid viscosity takes a value of about 0.0006. Therefore, we assume that the normal viscous stress at the gas side of the interface can be neglected. Then Eq. (1) yields the following relation for the non-dimensional local interface curvature, K,

$$K \equiv \kappa D_h \approx \frac{D_h}{\sigma}\left(p_{L,i} - p_B + \tau^{\perp}_{L,i} \right) \tag{5}$$

When the bubble moves either in positive or negative y-direction (unit vector $\mathbf{e}_y$), then the dyadic product at the bubble front and rear becomes $\mathbf{n}_i\mathbf{n}_i = \mathbf{e}_y\mathbf{e}_y$ and we have with $\mathbf{v}_L = (u_L, v_L, w_L)^T$ for the normal viscous stress on the liquid side of the interface at the bubble tip and rear the relation

$$\begin{aligned} \tau^{\perp}_{L,tip/rear} &= \mu_L \left(\nabla\mathbf{v}_L + (\nabla\mathbf{v}_L)^T \right)\Big|_{tip/rear} : \mathbf{e}_y\mathbf{e}_y \\ &= 2\mu_L \left.\frac{\partial v_L}{\partial y}\right|_{tip/rear} \end{aligned} \tag{6}$$

The velocity gradient in y-direction in the liquid phase at the bubble tip and rear may be approximated as (see Fig. 4)

$$\left.\frac{\partial v_{\mathrm{L}}}{\partial y}\right|_{\mathrm{tip}} \approx -\left.\frac{\partial v_{\mathrm{L}}}{\partial y}\right|_{\mathrm{rear}} \approx \frac{U_{\mathrm{L,cl}} - U_{\mathrm{B}}}{L_{\mathrm{nvbl,tip/rear}}} \tag{7}$$

Here, $U_{\mathrm{L,cl}}$ is the magnitude of the axial velocity in the liquid slug on the channel centerline and L_{nvbl} is the axial distance across which this velocity change occurs. For a fully developed liquid slug the axial centerline velocity is given by

$$U_{\mathrm{L,cl}} = C_{\square} J_{\mathrm{tot}} = 2.0962 J_{\mathrm{tot}} \tag{8}$$

Here, $J_{\mathrm{tot}} \equiv \varepsilon\, U_{\mathrm{B}} + (1 - \varepsilon)\, U_{\mathrm{L}}$ is the total superficial velocity. U_{L} denotes the magnitude of the mean axial liquid velocity within the unit cell. Using Eq. (8) and defining $\psi \equiv U_{\mathrm{B}}/J$ we can write

$$K_{\mathrm{tip}} \approx \frac{D_{\mathrm{h}}(p_{\mathrm{B}} - p_{\mathrm{L,tip}})}{\sigma} + \frac{2D_{\mathrm{h}}}{L_{\mathrm{nvbl,tip}}} Ca \left(\frac{C_{\square}}{\psi} - 1 \right) \tag{9}$$

and

$$K_{\mathrm{rear}} \approx \frac{D_{\mathrm{h}}(p_{\mathrm{B}} - p_{\mathrm{L,rear}})}{\sigma} - \frac{2D_{\mathrm{h}}}{L_{\mathrm{nvbl,rear}}} Ca \left(\frac{C_{\square}}{\psi} - 1 \right) \tag{10}$$

Thus, the effect of the normal viscous stress on the curvature of the bubble front and rear depends on the ratio $C_{\square} / \psi$. For recirculation flow it is $\psi < C_{\square}$ and the normal viscous stress acts to increase the curvature of the bubble tip and to decrease the curvature of the bubble rear. For $\psi > C_{\square}$ we have bypass flow and Eqs. (9) and (10) suggest that the curvature of the bubble tip is decreasing with increase of Ca, while that of the bubble rear is increasing. Here, we have always $\psi < C_{\square}$ and the second term on the r h.s. of Eq. (9) is positive.

Combining Eqs. (9) and (10) yields

$$K_{\mathrm{tip}} - K_{\mathrm{rear}} \approx \frac{D_{\mathrm{h}}(p_{\mathrm{L,rear}} - p_{\mathrm{L,tip}})}{\sigma} + 2Ca \left(\frac{C_{\square}}{\psi} - 1 \right) \left(\frac{D_{\mathrm{h}}}{L_{\mathrm{bl,tip}}} + \frac{D_{\mathrm{h}}}{L_{\mathrm{bl,rear}}} \right) \tag{11}$$

Thus, the difference in curvature of the front and rear meniscus depends on the pressure drop in the liquid phase over the length of the bubble. For a given pressure difference $p_{\mathrm{B}} - p_{\mathrm{L,tip}}$, this difference in curvature increases with increase of Ca for $\psi < C_{\square}$ and decreases with increase of Ca for $\psi > C_{\square}$ where ψ itself is a function of Ca.

With exception of the bubble front and rear stagnation point, the normal viscous stresses may be neglected. Then, the following relation for the local curvature at an arbitrary point $\mathbf{x}_{\mathrm{i}}$ lying on the interface should approximately hold

$$K(\mathbf{x}_{\mathrm{i}}) = \frac{D_{\mathrm{h}}}{\sigma} \left(p_{\mathrm{B}} - p_{\mathrm{L}}(\mathbf{x}_{\mathrm{i}}) \right) \tag{12}$$

Thus, the knowledge of the pressure field on the liquid side of the interface is the key to understand the bubble shape. Since variations of the pressure in the channel cross-section are related to the velocity field, we investigate in the next subsection both, the local pressure field and the local velocity field.

Analysis of local pressure and velocity field

Figure 3 shows for case 4_20_B of Keskin et al. (2010) the axial profile of the pressure for different positions within the channel cross-section. While in the governing equations adding a constant to the pressure field is without influence as only the pressure gradient matters, in Figure 3 for clarity of presentation a constant has been added to the pressure values so that the minimum pressure at the bottom of the channel (y = 0) is zero. From Figure 3 it is evident that in the liquid slug the pressure within an axial cross-section is uniform as it is typical for laminar single phase flow in a straight channel. Furthermore, in the liquid slug the axial pressure drop is constant. Figure 3 also shows that the pressure in the bubble is about constant (see profile for channel centerline in the range y = 2 – 4 mm). It further indicates that a notable variation of the pressure within an axial cross-section occurs only at the bubble rear. There, the pressure difference between the bubble and the liquid is clearly larger in the lateral film region than in the corner flow region. At the rear edge of the interface the normal viscous stresses may be neglected; therefore for this region Eq. (12) may be used to estimate the local interface curvature. As Figure 3 shows the difference between the pressure in the bubble and on the liquid side of the interface is finite in lateral direction, whereas it is almost zero in diagonal direction. According to Eq. (12), therefore, the local interface curvature close to the center of the channel side walls is finite (and positive) while it is about zero in diagonal direction. This explains the cross-sectional interface shape as given by the red line in Figure 2b).

Figure 3 shows that the axial pressure drop in the liquid phase across the bubble length occurs to the main part over the first third of the bubble. In the region, where the thickness of the lateral liquid film is about constant, the pressure is nearly constant too, and no significant axial pressure drop exists.

It is obvious that in the bubble region the pressure field is closely related to the velocity field. Hazel & Heil (2002) analyzed the steady propagation of a semi-infinite bubble into a channel of rectangular cross-section by solving the free-surface Stokes equations and investigated in detail the pressure and velocity field in the liquid phase in axial cross-sections at various distances from the bubble tip. They found that in square channels the fluid particles tend to move towards the corners, which offer less resistance to the flow than the thinner regions along the sides of the channel. The ensuing transverse flows induce a transverse pressure gradient that lowers the fluid pressure in the corners, where the gas-liquid interface moves radial outwards. In the region behind the bubble tip, surface tension acts to restore the gas-liquid interface to an axisymmetric shape, and the non-uniform pressure distribution continues to drive fluid into the corner until the bubble diameter in lateral and diagonal direction are equal. As concerns the case 4_20_B, Figure 3 shows that in axial regions which are closer to the bubble tip than to the bubble rear, the pressure within a certain axial cross-section is indeed slightly lower in the corners than at the channel sides. However, in axial cross-sections which are closer to the bubble rear than to the bubble tip, we find the opposite behavior, i.e. higher pressure values in the channel corners than at the channel sides.

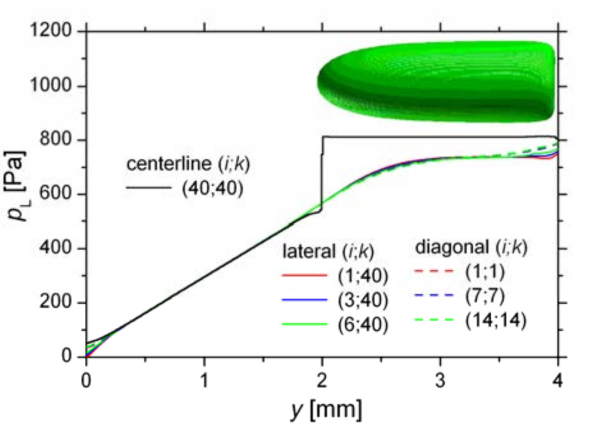

Figure 3: Axial profile of pressure at different positions in the channel-cross section for case 4_20_B in Keskin et al. (2010). The values (i,k) denote the mesh cell index within the channel cross-section ($1 \le i \le 80$; $1 \le k \le 80$).

In Figure 4 we show axial profiles of the liquid axial velocity at different positions within the channel cross-section. We find that the axial liquid velocity is, as expected, in general higher in the corner region than in the lateral liquid film region. However, at a position close to the bubble rear and close to the interface the liquid axial velocity is about the same in lateral and diagonal direction (compare in Figure 4 the profile for $i = k = 14$ with the one for $i = 7$, $k = 40$ at $y \approx 4$mm). A comparison of the velocity components within the channel-cross section (not shown here) indicates that the magnitude of the liquid velocity in the cross-section is higher in the channel corners than at the channel sides. Thus, in a cross-section close to the bubble rear the liquid moves faster inward in the channel corners than at the channel sides. This inward directed liquid flow is associated with curved streamlines, which result in the presence of non-negligible inertial forces in a non-uniform cross-sectional pressure distribution which has, in the present case, maxima in the channel corners. However, further investigations are needed to elucidate the intimate relation between the local pressure and velocity fields and the interface curvature at the bubble rear.

From Figure 4 we can evaluate the length L_{nvbl} and find $L_{\mathrm{nvbl,tip}} / D_h \approx 0.2$ and $L_{\mathrm{bl,rear}} / D_h \approx 0.16$, respectively. With these data, the numerical values of the different terms in Eqs. (9) and (10) become

$$K_{\mathrm{tip}} \approx \frac{0.001\mathrm{m}(812\mathrm{Pa}-541\mathrm{Pa})}{0.0286\mathrm{N/m}} + \frac{2}{0.2}0.655\left(\frac{2.096}{1.96}-1\right) = 9.475 + 0.455 = 9.93 \tag{13}$$

and

$$K_{\mathrm{rear}} \approx \frac{0.001\mathrm{m}(812\mathrm{Pa}-770\mathrm{Pa})}{0.0286\mathrm{N/m}} - \frac{2}{0.16}0.655\left(\frac{2.096}{1.96}-1\right) = 1.468 - 0.568 = 0.9 \tag{14}$$

While these values should be considered as estimates of the magnitudes of the relevant forces, they nevertheless show that in the present case 4_20_B the curvature of the bubble tip is one order of magnitude larger than the one at the bubble rear. Furthermore it is evident that at the bubble tip the normal viscous stresses are one order of magnitude smaller than the pressure forces, while at the bubble rear the magnitude of the normal viscous stresses is about 38% of that of the pressure forces. Since at the bubble rear the normal viscous stresses on the liquid side of the interface act opposite to the pressure forces for $\psi < C_{\square}$, they are definitely important and should not be neglect at high values of the capillary number.

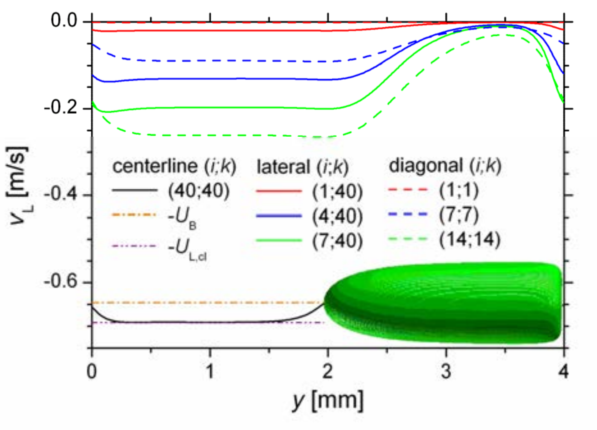

Figure 4: Axial profile of liquid axial velocity at different positions in the channel-cross section for case 4_20_B in Keskin et al. (2010). The values (i,k) denote the mesh cell index within the channel cross-section ($1 \le i \le 80$; $1 \le k \le 80$).

Transition from slug to annular flow

In this subsection we present and discuss results of a new transient simulation for a square mini-channel, where the pressure gradient is so high that co-current downward Taylor flow is not stable and a transition from slug flow to annular flow occurs. In this simulation it is $L_{\mathrm{uc}} = 4$ mm and $\varepsilon = 0.4$; we denote this case by 4_40_C. The initial bubble shape is displayed in Figure 6. The initial velocity is the same in both phases and is constant, namely $v_L = v_G = -0.3$ m/s. The prescribed mean pressure difference between the top and bottom cross-section of the channel is for this case 550.3 Pa. This value is about 27% lower than for case 4_20_B, where it is 754.4 Pa. However, the hydrostatic pressure head that must be overcome to drive the flow downward is much lower for case 4_40_C. This is because the gas holdup is 40% instead of 20% for case 4_20_B.

Figure 5 shows the temporal evolution of J_{tot}, U_B and U_L during the course of the simulation. As can be seen, the downward velocity of the bubble strongly increases in time whereas the magnitude of the mean liquid velocity in the domain is slightly decreasing. At about 5 ms the slope of U_B versus t decreases somewhat before it is strongly increasing for $t > 8$ ms. Thus, the bubble velocity approaches no constant value; instead the bubble is always accelerating.

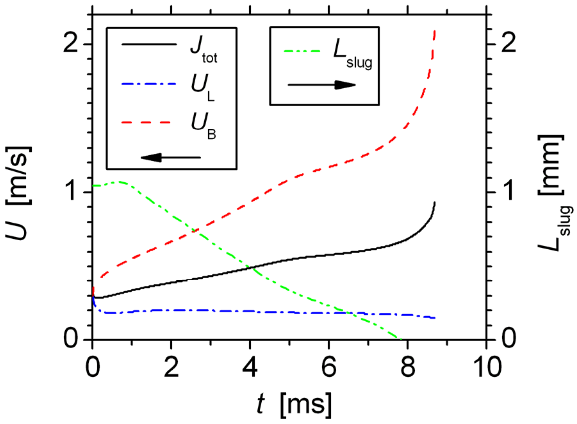

Figure 5: Transition from Taylor flow to annular flow: temporal evolutions of total superficial velocity, bubble velocity, mean liquid velocity and liquid slug length for case 4_40_C.

Also shown in Figure 5 is the time history of the liquid slug length L_{slug}. For each instant in time, this length is evaluated as the axial distance along which in the entire channel cross-section only liquid is present. The initial liquid slug length is about 1 mm. At $t = 5$ ms this value is reduced to about 0.3 mm while for $t > 8$ ms its value is zero.

Figure 6 shows the bubble shapes for case 4_40_C at 12 different instants in time. As time proceeds we observe that the rear meniscus of the bubble quickly deforms from the initially hemispherical shape to a flat interface, which is reached at $t \approx 2$ ms. Characteristic for the time period from $t = 2 - 5$ ms is a concave rear meniscus on the channel axis which goes along with a non axi-symmetric bubble shape in some radial distance from the channel centerline. This bubble shape will be discussed below. As time proceeds further, the diameter of the bubble body continues to decrease while the length of the bubble increases and accordingly the length of the liquid slug decreases. As a consequence of the decreasing bubble diameter, the flow along the circumferential of the bubble becomes more uniform because the difference in the axial velocity on the liquid side of the interface in the lateral liquid film and the liquid corner flow diminishes. Due to this, in the time period $t = 5 - 8$ ms the rear meniscus is almost axisymmetric again. For $t > 8$ ms the liquid slug length is zero and the tip of the trailing bubbles penetrates in the concave region of the rear meniscus of the trailing bubble. At this stage the present simulation breaks down. The reason is that during the process of the merger of the trailing and leading interfaces a large number of small gas and liquid fragments are produced. The curvature of these tiny structures cannot adequately be resolved by the grid.

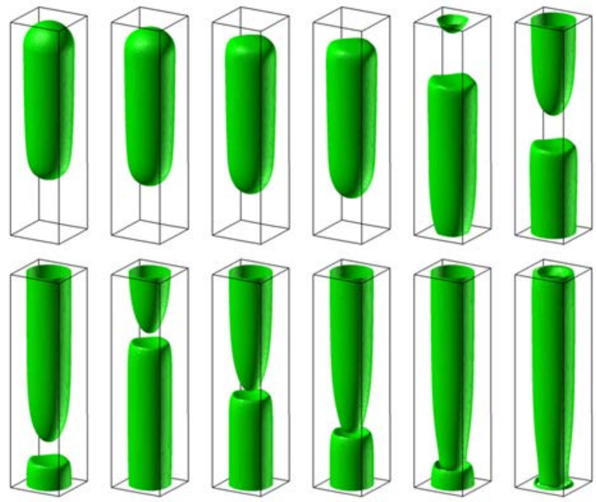

Figure 6: Visualization of instantaneous bubble shape for case 4_40_C during the transition from Taylor flow to annular flow for different instants in time. Top row (from left to right): 0 ms, 0.27 ms, 0.53 ms, 0.67 ms, 1.93 ms, 3.72 ms; bottom row (from left to right): 5.05 ms, 6.65 ms, 7.45 ms, 7.99 ms, 8.42 ms, 8.62 ms.

a) b)

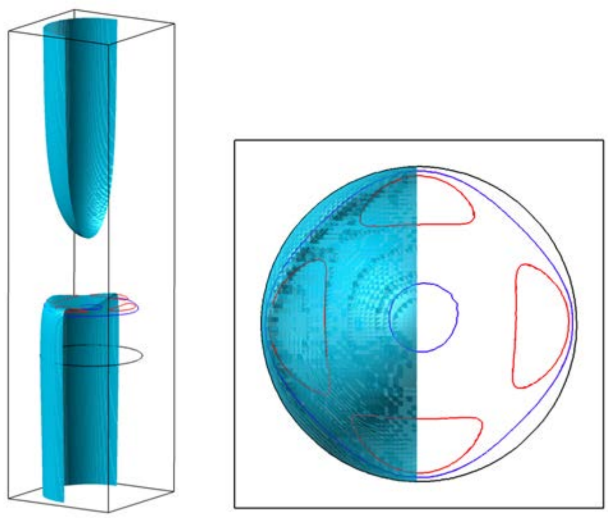

Figure 7: Bubble shape for case 4_40_C at $t = 3.72$ ms in a) perspective view and b) view from front (only one half of the bubble is shown). The three lines indicate the bubble shape in an axial cross-section in the middle of the bubble (black line) and close to the bubble rear (blue and red line).

In Figure 7 we investigate the shape of the bubble rear for t = 3.72 ms in more detail. Similar to Figure 2 we display the shape of the interface in the channel cross-section at certain axial positions. It is evident that the body of the bubble is axi-symmetric (black line in Fig. 7 b). Close to the bubble rear we find again the characteristic shape of a square with rounded corners (blue line) that was already found for case 4_20_B, see Fig. 2 b). However, as indicated by the small blue circle, in the present case the interface at the rear meniscus is not flat but slightly concave. In an axial position slightly more upstream we find four closed iso-lines of the bubble interface (red lines). These represent cusps that form where the bubble rear is close to the middle of the lateral four walls of the vertical channel. A detailed inspection of Fig. 7b) shows that the red and blue lines are not perfectly symmetric with respect to the vertical channel mid-planes or the channel diagonals (note that our simulation is full 3D and no kind of symmetry is assumed). Instead, the respective patterns slightly change in time. We speculate that these interface deformations and fluctuations are due to the continuous acceleration of the bubble. It is an open question if such a shape of the rear meniscus may persist under steady bubble motion. To investigate this issue, a new simulation is currently under way where we take the final time step of case 4_20_B as initial condition, but increase the driving pressure difference by about 10%.

Conclusions

In this paper we used results of three-dimensional numerical simulations of viscous co-current downward Taylor flow in a square vertical mini-channel to investigate the shape of the front and rear meniscus at different values of the capillary number. It is found that the curvature of the front meniscus increases with increase of Ca while that of the rear meniscus decreases. This behavior is in qualitative agreement with that in circular channels. For the highest capillary number, Ca = 0.65, we find a novel non-axisymmetric bubble shape regime which has – to the author's knowledge – not been reported so far. This new regime is characterized by a bubble shape which is axisymmetric at the tip and body of the bubble but adopts the shape of a square with rounded corners at the bubble rear. We showed that this symmetry breaking is related to a non-uniform pressure distribution in cross-sections close to the rear meniscus, with local pressure maxima in the channel corners.

We also investigated the evolution of the bubble shape during the transition from Taylor flow to annular flow in a square channel. During this transient simulation, the bubble is always accelerating and the diameter of the axisymmetric bubble body decreases in time while the length of the bubble increases. In certain stages of this simulation the rear meniscus shows the novel shape described above and even forms cusps close to the middle of the four channel side walls. However, it is unclear if the latter shape exists only when the bubble accelerates or also under steady bubble motion.

Nomenclature

Ca	Capillary number (–)
D_h	hydraulic diameter (m)
$\mathbf{e}_y$	unit normal vector in axial direction (–)
g	gravitational constant (m/s^2)
H	mean interface curvature (1/m)
i	mesh cell index in x-direction (–)
J_{tot}	total superficial velocity (m/s)
j	mesh cell index in y-direction (–)
K	non-dimensional interface curvature (–)
k	mesh cell index in z-direction (–)
La	Laplace number (–)
L_{nvbl}	thickness of normal viscous boundary layer (m)
L_{slug}	length of the liquid slug (m)
L_{uc}	Length of the unit cell (m)
$\mathbf{n}_i$	unit normal vector to the interface (–)
p	pressure (N/m^2)
R_{min}	minimum principal radius of curvature (m)
R_{max}	maximum principal radius of curvature (m)
Re	Reynolds number (–)
U_B	magnitude of bubble velocity (m/s)
U_L	magnitude of mean liquid velocity (m/s)
$\mathbf{v}$	velocity field (m/s)
x	wall-normal coordinate (m)
We	Weber number (–)
y	axial coordinate (positive in upw. direction) (m)
$\mathbf{x}$	Cartesian coordinates, $\mathbf{x} = (x,y,z)^T$ (m)
z	wall-normal coordinate (m)

Greek letters

ε	gas holdup in computational domain (–)
κ	interface curvature (1/m)
μ	dynamic viscosity (Pa s)
σ	coefficient of surface tension (N/m)
ψ	$= U_B / J_{tot}$ (–)
$\tau^{\perp}$	normal viscous stress (Pa)

Subscripts

B	bubble
G	gas phase
i	interface
L	liquid phase
nvbl	normal viscous boundary layer
rear	rear meniscus on channel axis
tip	front meniscus on channel axis
uc	unit cell

References

Bauer, T. Experimental and theoretical investigations of monolithic reactors for three-phase catalytic reactions. PhD thesis, Technical University Dresden, 2007.

Giavedoni, M.D., Saita, F.A. The rear meniscus of a long bubble steadily displacing a Newtonian liquid in a capillary tube. Phys. Fluids **11** (1999) 786.

Günther, A., Jensen, K.F. Multiphase microfluidics: from flow characteristics to chemical and material synthesis. Lab Chip **6** (2006) 1487.

Hazel, A.L., Heil, M. The steady propagation of a semi-infinite bubble into a tube of elliptical or rectangular cross-section. J. Fluid Mech. **470** (2002) 91.

Kececi, S., Wörner, M., Onea, A., Soyhan, H.S. Recirculation time and liquid slug mass transfer in co-current upward and downward Taylor flow. Catalysis Today **147S** (2009) S125.

Keskin, Ö., Wörner, M., Soyhan, H.S., Bauer, T., Deutschmann, O., Lange, R. Viscous co-current downward Taylor flow in a square mini-channel. AIChE J., in press, doi: 10.1002/aic.12113.

Kreutzer, M.T., Kapteijn, F., Moulijn, J.A., Heiszwolf, J.J. Multiphase monolith reactors: chemical reaction engineering of segmented flow in microchannels. Chem. Eng. Sci. **60** (2005) 5895.

Martinez, M.J., Udell, K.S. Boundary integral analysis of the creeping flow of long bubbles in capillaries. J. Appl. Mech. **56** (1989) 211.

Öztaskin, M.C., Wörner, M., Soyhan, H.S. Numerical investigation of the stability of bubble train flow in a square minichannel. Phys. Fluids **21** (2009) 042108.

Sabisch, W., Wörner, M., Grötzbach, G., Cacuci, D.G. 3D volume-of-fluid simulation of a wobbling bubble in a gas-liquid system of low Morton number. 4th Int. Conf. Multiphase Flow, ICMF-2001, New Orleans, LA, USA, May 27 – June 1, 2001, CD-ROM.

Taha, T., Cui, Z.F.. CFD modelling of slug flow inside square capillaries. Chem. Eng. Sci. **61** (2006) 665.

Taylor, G.I. Deposition of a viscous fluid on the wall of a tube. J. Fluid Mech. **10** (1961) 161.

Thulasidas, T.C., Abraham, M.A., Cerro, R.L. Bubble-train flow in capillaries of circular and square cross section. Chem. Eng. Sci. **50** (1995) 183.

Thulasidas, T.C., Abraham, M.A., Cerro, R.L. Flow patterns in liquid slugs during bubble-train flow inside capillaries. Chem. Eng. Sci. **52** (1997) 2947.